Geochemistry, Geophysics, Geosystems®

AGU ADVANCING EARTH AND SPACE SCIENCES

RESEARCH ARTICLE
10.1029/2024GC011535

Sulfide Melt Wetting Properties in Earth's Mantle: New Constraints From Combined 2D and 3D Imaging

C. Beyer[1], R. O. C. Fonseca[1], T. Bissbort[2], L. Schröer[3], and V. Cnudde[3,4]

[1]Inst. for Geology, Mineralogy and Geophysics, Ruhr-Universität Bochum, Bochum, Germany, [2]Dept. of Earth and Environmental Sciences, Ludwig-Maximilians-Universität München, Munich, Germany, [3]PProGRess-UGCT, Department of Geology, Ghent University, Ghent, Belgium, [4]Environmental Hydrogeology, Department of Earth Sciences, Utrecht University, Utrecht, The Netherlands

Key Points:

- The mobility of mattes is enhanced by majoritic garnet at sub-lithospheric depths
- The combination of 2D and 3D methods improves our understanding of liquid percolation in the Earth's mantle

Supporting Information:

Supporting Information may be found in the online version of this article.

Correspondence to:

C. Beyer,
christopher.c.beyer@rub.de

Citation:

Beyer, C., Fonseca, R. O. C., Bissbort, T., Schröer, L., & Cnudde, V. (2024). Sulfide melt wetting properties in Earth's mantle: New constraints from combined 2D and 3D imaging. *Geochemistry, Geophysics, Geosystems*, *25*, e2024GC011535. https://doi.org/10.1029/2024GC011535

Received 29 FEB 2024
Accepted 1 MAY 2024

Author Contributions:

Conceptualization: C. Beyer, R. O. C. Fonseca
Formal analysis: C. Beyer, T. Bissbort, L. Schröer
Funding acquisition: C. Beyer, R. O. C. Fonseca
Investigation: C. Beyer, R. O. C. Fonseca
Resources: L. Schröer, V. Cnudde
Visualization: C. Beyer, T. Bissbort
Writing – original draft: C. Beyer, R. O. C. Fonseca
Writing – review & editing: C. Beyer, T. Bissbort, L. Schröer, V. Cnudde

Abstract Base-metal sulfur liquids (mattes) play a crucial role as metasomatic agents and carriers of highly siderophile elements (HSE) within the Earth's mantle. Prior research has predominantly focused on sulfur-poor metallic liquids involved in core formation scenarios. We conducted high-pressure experiments using a multi-anvil apparatus to investigate the effects of pressure, non-ferrous compounds in mattes, and the mineral composition of the silicate host on matte wetting properties. Specifically, we explored conditions representing both the lithospheric (6 and 7 GPa) and sub-lithospheric Earth's mantle (13 GPa). We characterized the experiments using the distribution of the dihedral angle in backscattered-electron sections and the sphericity and network topology of the mattes in tomography scans. Our findings reveal distinct behaviors: while the matte in olivine-dominated samples exhibited behaviors consistent with previous studies, such as high dihedral angle values (94° and 100°), the majorite-bearing sample run at 13 GPa formed a disseminated network with a mean dihedral angle of 43°, below the connectivity threshold of 60°. Furthermore, in an experiment involving a garnet-bearing silicate host, we observed a decrease in the matte's dihedral angle to 72°. Our results suggest that pressure within mafic hosts contributes to increased matte mobility in the sub-lithospheric Earth's mantle, especially inasmuch as the stability of garnet phases is concerned. Consequently, mattes within subducted oceanic crusts may efficiently transport HSE into surrounding lithologies, while mattes within depleted, more harzburgitic lithologies and the ambient mantle may remain trapped within the silicate host at low melt fractions.

Plain Language Summary Our study focused on how sulfur-rich liquids percolate in Earth's mantle and carry important elements. Previous research mostly studied how metallic liquids, which are sulfur-poor, form planetary cores. We did experiments under high pressure and high temperature to see how different factors affect the mobility of sulfur-bearing liquids in the deep Earth's mantle. We found that the type of rock and pressure levels affect how mattes spread. When rocks contained the high-pressure polymorph of garnet, called majorite, mattes moved differently compared to rocks that mostly contain the mineral olivine. Our results show that rocks and pressure levels influence matte movement in regions of Earth's mantle that are comprised of subducted oceanic crust. This helps us understand how elements move inside the Earth, especially when oceanic crust sinks into the mantle.

1. Introduction

Base metal sulfide liquids (e.g., Fe-Ni-Cu-S-O) exhibit distinctive characteristics compared to those of silicate melts. They feature a higher density and lower viscosity compared to silicate melts, and may have a significant effect on the rheology of regions of the mantle where sulfides are molten (Helffrich et al., 2011). Recent research has further demonstrated that sulfides can exist in at least a partial molten state across a wide range of pressure and temperature conditions within the Earth's upper mantle and upper transition zone. The persistence of sulfide liquid is primarily a function of its chemical composition, as elucidated by Beyer et al. (2022) and Zhang and Hirschmann (2016). In addition to their physico-chemical attributes, sulfide melts play a pivotal role as the primary hosts for highly siderophile elements within the Earth's mantle (Lorand & Luguet, 2016; Luguet et al., 2003, 2007). Consequently, the mobility of sulfide melts holds significant implications for the cycling of chalcophile and siderophile elements in the deep Earth. Whether a liquid wets a surface and possesses the ability to move along grain boundaries depends on the ratio of surface energies between the liquid and solid. Commonly,

this is expressed as the wetting angle, also referred to as the dihedral angle (Θ), and represents the equilibrium angle at the triple junction of two grains and a liquid.

$$2\cos\frac{\Theta}{2}=\frac{\gamma_{ss}}{\gamma_{sl}} \quad (1)$$

where γ_{ss} and γ_{sl} are the solid-solid and solid-liquid surface energies, respectively. Strictly speaking, Equation 1 is only applicable to texturally equilibrated monomineralic systems if the interfacial energies are isotropic. This expression can be used to determine whether a liquid forms an interconnected network or becomes trapped in isolated pockets along grain boundaries. It thus serves as a proxy for the mobility of a liquid (or melt) within the host rock matrix. von Bargen and Waff (1986) demonstrated that independently of the liquid fraction, a liquid will form interconnected channels when $0° < \Theta < 60°$. Dihedral angles greater than 60° require a critical liquid fraction to achieve connectivity. Slightly below the critical melt fraction is the pinch-off melt fraction. The pinch-off melt fraction is a finite amount of non-wetting melt ($\Theta > 60°$) that increases with increasing Θ and remains in isolated pockets and is trapped along grain boundaries (von Bargen & Waff, 1986). Generally speaking, the higher the value of Θ, the higher the critical liquid fraction necessary to maintain full liquid connectivity along grain boundaries. In-situ electrical conductivity studies on liquids like metallic melts in a silicate matrix indicate a connectivity threshold of around 5 vol.% for Θ values above 60° (Yoshino et al., 2003), with some researchers advocating for even higher values (Bagdassarov et al., 2009; Walte et al., 2007).

Previous experimental studies have used the dihedral angle almost exclusively to determine the wetting properties of iron-sulfur liquids in contact with silicates (Ballhaus & Ellis, 1996; Gaetani & Grove, 1999; Minarik et al., 1996; Roberts et al., 2007; Rose & Brenan, 2001; Shannon & Agee, 1996, 1998; Terasaki et al., 2005). Oxygen and sulfur have been found to decrease the wetting angle of these liquids and thus enhance melt mobility and its percolation (Gaetani & Grove, 1999; Minarik et al., 1996; Terasaki et al., 2008). The majority of studies used monomineralic matrices mostly consisting of olivine or its polymorphs (e.g., ringwoodite). To our knowledge, only Brenan and Rose (2002), investigated the wetting properties of sulfide melt with a matrix other than silicates by using chromite. Shannon and Agee (1996) reported wetting angles between pyroxenes and sulfur-bearing metallic liquid, which were similar to those reported for olivine - metallic liquid wetting angles from the same experiment (4° difference). The only study on pyrope-rich garnet ($Py_{63}Alm_{24}Grs_{13}$) on the wetting properties of sulfur-bearing iron melts showed no discernible effect of pressure (at 5 GPa—Gilpin et al. (2002)). In addition, the presence of silicate melt showed no effect on the wetting behavior of sulfur-bearing iron liquid (Fe-FeS eutectic composition) at conditions of Earth's upper mantle (Cerantola et al., 2015; Holzheid, 2013; Holzheid et al., 2000).

The advent of X-ray computed tomography (μCT) and its use to the study of the percolation of natural sulfide melts in igneous cumulates and ore deposits, has provided valuable insights into the topology of sulfides and sulfide melt (Barnes et al., 2008, 2011; Godel, 2013; Godel et al., 2006). However, it had not been extensively utilized in experimental melt percolation experiments until recently, when researchers studied the geometry of liquid Fe-S in an olivine matrix (Berg et al., 2017; Kono et al., 2023) and Shi et al. (2013), who studied the percolation of iron melt in a bridgmanite matrix in a diamond-anvil cell at conditions of the Earth's lower mantle. Despite these recent advancements, most studies have focused on planetary core formation scenarios, where the melt composition is typically metallic with high molar metal/S ratios of above 1.5, which is close to the Fe-FeS eutectic (Ballhaus & Ellis, 1996; Berg et al., 2017; Minarik et al., 1996; Roberts et al., 2007; Shannon & Agee, 1998). There has been limited exploration of melt migration involving magmatic sulfide compositions (metal/S ∼1) and matrix components like garnet, majorite and sodic clinopyroxenes, which are common in the Earth's mantle. Understanding the segregation of magmatic sulfide liquids in these host lithologies is crucial for gaining insights into the transport of siderophile and chalcophile elements (Fonseca et al., 2024; Gaetani & Grove, 1999; Rose & Brenan, 2001). Furthermore, to our knowledge, the effect of non-ferrous components (Ni, Cu, and Co) on the dihedral angle has only been systematically studied by Rose and Brenan (2001). Rose and Brenan (2001) discovered that non-ferrous transition metals have a significant impact on the dihedral angle at low oxygen fugacities (approximately two to three orders of magnitude more reducing than the fayalite-magnetite-quartz reference redox equilibrium—FMQ), resulting in an increased apparent dihedral angle. Conversely, under more oxidizing conditions (FMQ-0.7), the presence of non-ferrous components was observed to have no discernible effect on the wetting angle. However, Rose and Brenan (2001) carried out their experiments at 1300°C

Table 1
Bulk Starting Compositions Measured by Microprobe

wt.%	Harzburgite Monastery Mine	Eclogite Dora Maira Massif	MORB glass Beyer et al. (2021)
SiO_2	43.6	46.19	51.98
TiO_2	0.1	2.7	–
Al_2O_3	1.32	13.54	15.97
Fe_2O_3			1.00[a]
FeO	7.12[b]	13.15[b]	8.96
MnO	0.1	0.21	–
MgO	40.4	5.56	7.87
CaO	0.99	10.97	11.7
Na_2O	0.12	2.75	2.52
K_2O	0.47	0.11	–
P_2O_5	0.03	0.31	–
H_2O	2.91	–	–
CO_2	0.85	–	–
		Sulfides	
wt.%	P1_x2	P3b_x2	E1_x2
Fe	35.68	30.75	53.86
Ni	25.56	31.25	6.32
Cu	0.82	1.32	0.81
S	37.95	36.83	38.52
O	0.15	0.18	0.07
Atomic frac.			
Cation/anion	0.91	0.95	0.90
Fe/Σmetals	0.59	0.50	0.89

[a]Mössbauer spectroscopy. [b]Total FeO.

and 0.1 MPa in a controlled gas atmosphere, conditions far removed from those prevalent in planetary interiors, so it is unclear whether their finds can be extrapolated to the higher pressure and temperature conditions of planetary mantles.

In this study, we seek to expand the study of the mobility of S-rich melts by investigating the influence of sulfide composition (Fe/Σmetals), mineral interior (including garnet, majoritic garnet, olivine, and pyroxenes), and pressure on the likelihood of sulfide melt to form an interconnected liquid network under lithospheric (6–7 GPa) and sub-lithospheric mantle (13 GPa) conditions at temperatures between 1450 and 1520°C. Additionally, we conducted experiments where sulfide melt coexisted with silicate melt to explore the impact of dual liquids on sulfide melt mobility. Our methodology involves utilizing 2D dihedral angles and 3D X-ray tomographic data to quantify the extent of melt connectivity and morphology.

2. Methods

2.1. Experimental Methods

A total of five multi-anvil experiments were carried out using different starting materials. These consisted of a mechanical mixture of synthetic Fe-Ni-Cu-S sulfides used in two previous studies (Beyer et al., 2022; Fonseca et al., 2024) and crushed natural harzburgite (sample 31181, Monastery Mine, South Africa), natural eclogite (Dora Maira Massif, Italy), and synthetic normal MORB glass (Beyer et al., 2021). The main difference between the sulfides is the Fe-Ni ratio (Table 1). The silicate rocks were only lightly crushed to a grain size between 3 and

Table 2
Experimental Run Conditions and Median Dihedral Angles

#	P [GPa]	T [°C]	Silicate matrix	Sulfide	Sil-sulf ratio [wt.%]	Sintering [h]	Supra liquidus [h]	Mean Θ [°]	CI^{-} [°]	CI^{+} [°]	# Angles
E358	6	1450	Harzburgite	P1_x2	93/7	7	12	94	92	96	202
E361	6	1450	Harzburgite	P3b_x2	93/7	21	12	100	95	104	131
E390[a]	13	1450	Eclogite	P3b_x2	93/7	20[b]	12	43	37	51	224
E390[c]	13	1450	Eclogite	P3b_x2	93/7	20[b]	12	99	94	102	147
E392	6	1450	Eclogite	P3b_x2	93/7	8	12	n.m.			
E394	7	1520	MORB glass	E1_x2	93/7	8	12	72	69	76	566

Note. The median and the 95% confidence interval (CI) were calculated using bootstrapping of 1,000 samples. n.m. not measured. [a]Melt network. [b]Sintering at 1350°C to obtain a majorite-bearing eclogite phase assemblage. [c]Isolated pockets.

70 μm. Sulfide and silicate components were mixed in a 7:93 weight ratio by gently mixing them with an agate mortar and pestle for at least 30 min.

The experiments were conducted using a 630-ton Walker-type multi-anvil apparatus at Ruhr-University Bochum, operating at pressures of 6, 7, and 13 GPa and temperatures of 1450–1520°C. The multi-anvil press was calibrated against well-known phase transitions and the calibration is checked regularly at least twice a year. The pressure accuracy was ±0.5 GPa. Details on the calibration procedure and assembly design are given in Beyer et al. (2022). Each experiment underwent gradual compression, taking four to 5 hours to reach the target pressure. The first step involves sub-solidus sintering in the temperature range of 800–1000°C, lasting between 7 and 8 hr, to diminish capsule porosity and prevent sulfide liquid loss along cracks or grain boundaries. Following this, the temperature was increased to the desired target value at a rate of 100°C/min and maintained at that level for the specified duration (see Table 2). Quenching was achieved by disconnecting electrical power, causing the temperature to rapidly drop below 80°C within a few seconds. For experiment E390, we deviated from this procedure to crystallize majoritic garnet before the sulfide was molten. As such, we performed a second sintering step during experiment E390, at 1350°C and 13 GPa for 20 hr, to promote the formation of majoritic garnet, which only forms above pressures of 5 GPa (Irifune, 1987).

We used 14/8 (14 mm octahedron edge length, 8 mm truncated edge length) octahedral pressure media at 6 and 7 GPa and 10/4 octahedral pressure media at 13 GPa. The octahedra consisted of magnesium oxide doped with Cr_2O_3, sourced from *Ceramic Substrates*, Isle of Wight, and zirconium oxide insulators (*OZ8C*, *Mino Ltd*., Japan). Depending on pressure conditions, stepped graphite heaters (6 and 7 GPa) or 50 μm thick rhenium-foil heater (13 GPa) were used. Crushable MgO (RM98TE, *Rauschert GmbH*) and ZrO_2 (10/4) plugs were used within the pressure medium (Beyer et al., 2022). To monitor temperature, a type-D thermocouple was inserted axially using a quadbore alumina tube, which was further surrounded by a crushable MgO sleeve. The sample containers were milled from single-crystal MgO. To satisfy the requirements for high-resolution μCT, the inner diameter of the capsules was 1 mm and the length was 1.3 mm. The capsule were closed with a 0.8 mm thick MgO single-crystal lid.

To prevent sample deformation, which can potentially affect melt mobility (Cerantola et al., 2015; Groebner & Kohlstedt, 2006), we employed crushable MgO around the single crystal MgO capsule and crushable MgO rings at the ends of the ZrO_2 thermal insulator sleeve to promote hydrostatic conditions. Additionally, the experiments were conducted at high temperatures (1450–1520°C) for more than 12 hr, facilitating the decay of residual stress from the initial cold compression stage (Rubie, 1999).

After each experiment, MgO capsules and the sample inside were carefully extracted from the pressure assembly and mounted on a 0.7 mm diameter graphite pin for subsequent CT scanning. The sample diameter was trimmed to 0.8–1.2 mm. Following μCT analysis, the samples were embedded longitudinally in epoxy and polished with a succession of diamond pastes down to 0.25 μm for electron microscopy. To ensure that we exposed an adequate number of solid-liquid interfaces (>100), we repeated the polishing process twice and took measurements of the dihedral angle on each exposed surface. We also repeated the angle measurements twice for two random samples to gauge the potential bias introduced by manually measuring the angles.

2.2. Analytical Methods

The examination of the textures of sulfide phases in each experimental run involved scanning electron microscopy (SEM) and μCT. A JEOL JSM-7200F SEM situated at the Center for Interface-Dominated High-Performance Materials (ZGH) within Ruhr-University Bochum in Germany was used to perform multiple back-scattered electron (BSE) cross-sections of each sample. These BSE cross-sections were subsequently examined to obtain at least 100 dihedral angles per sample. Greyscale BSE images, with a magnification of at least 800X and an image resolution of 2500 × 1440 pixels were converted to binary images using the canny edge detection algorithm of the FeatureJ plugin package (https://imagescience.org/meijering/software/featurej/), which is implemented in ImageJ Fiji (Schindelin et al., 2012). The resulting image consists of lines representing the grain-melt and grain-grain interfaces. Additionally, we excluded sulfide melt pockets interfacing with cracks, gaps, and broken out edges from our measurements. The basic angle tool of ImageJ Fiji was used to manually determine the apparent dihedral angles between the silicates and the sulfide melt in these cross sections. Despite our efforts to ensure that measurements are as precise as possible, we estimate a potential error of 5°. This uncertainty is based on eight random angles that were measured five times each. The mean of the standard deviation of these repeated measurements was 4.7°.

The µCT scans were carried out at the Center of X-ray Tomography (UGCT) of Ghent University, Belgium, using Nanowood (Dierick et al., 2014). The setup with the open-type Hamamatsu transmission tube and large-area Varian detector was used. Each scan was acquired at 80 kV, 4 W, and without a filter. During one scan, 1,501 projections were taken at an exposure of 1,500 ms. Each projection consisted of three averages, and the total scan duration was about 2 hours. The scans were reconstructed using Octopus Reconstruction (XRE) using the in-house protocol. Spot, beam-hardening and ring filters were applied, just as a movement correction. The reconstruction parameters were kept constant as much as possible to allow easier comparison between the different data sets. The reconstruction produced a 16-bit stack of cross section (.tiff) representing the whole volume with a final voxel size of 0.9 µm. Image stacks were processed with Avizo 2022.2. In a first step, a cylindrical region of interest (ROI) was defined which excludes the MgO capsule and major decompression cracks. Subsequently, the image noise was reduced using a non-local means filter. The parameters were optimized to remove image artifacts while preserving enough information to easily segment the silicates and coexisting sulfides. As a quality check, we compared randomly picked reconstructed image slices with the BSE cross-sections. The filtered image was then segmented using either a global intensity threshold or a 2D-histogram threshold. Because of the high density contrast between silicates and sulfides, the segmentation yielded robust and reproducible results. Subsequently, the segmented binary image was separated to isolate individual grains. Material statistics were carried out on the segmented and separated volumes (melt pool volume and sphericity). The shape, or sphericity, of the sulfide melt pools is quantified using the factor Φ (Wadell, 1935).

$$\Phi = \frac{1}{A^3/\left(36 * \pi * V^2\right)}^{1/3} \tag{2}$$

where A is the surface area and V the volume of the melt pool in µm. A Φ of 1 represents a perfect sphere, with lower values indicating shapes that deviate from this ideal form. Values larger than 1 correspond to melt pools comprising only a few voxels, and are thus considered unrepresentative artifacts. Given our resolution of 0.9 µm per voxel we defined the minimum melt pool for the shape analysis with 300 μm^3. We found that this is the minimum size were the area integration in Avizo yields credible results.

To evaluate the extent of melt connectivity, we employed the Avizo skeletonization feature. This process generates a simplified network of interconnected nodes based on segmented and labeled CT volume reconstructions. We then utilized this network to compare the degree of melt connectivity across experiments. Nodes assigned a value of 1 denote terminated branches or isolated blebs, while those with a coordination number of three or higher indicate connected nodes. For a comprehensive explanation of this methodology, please refer to Godel (2013) and Miller et al. (2014). This method has the advantages over the use of the sphericity factor, because it is both less affected by artifacts that stem from the segmentation of the raw data, and also allows for the complete data set to be utilized.

A Cameca field emission SXFiveFE electron microprobe (EMPA) located at the Institute of Geology, Mineralogy, and Geophysics of the Ruhr-University Bochum (IGMG) was used to quantify the major element content

of the sulfide melt and silicates in each experiment. Measurements on the sulfide melt were carried out at an acceleration voltage of 15 kV and a beam current of 15 nA, employing a beam with a diameter ranging from 1 to 8 μm to account for any heterogeneity in the quenched sulfide melt. In order to avoid mixed analyses and mitigate secondary x-ray fluorescence from adjacent Fe-bearing phases, we measured the sulfide melt composition on blebs that were larger than 10 μm in diameter where possible. The counting times were between 15 and 30 s for the peaks and half of the peak counting times were used to measure the background. For calibration purposes, we used reference materials including chalcopyrite and Ni-metal to calibrate for S, Fe, Cu, and Ni, respectively, using peak-to-background calibrations. The determination of oxygen content was referenced to periclase, with oxygen backgrounds monitored by carrying out measurements on nominally oxygen-free phases such as metals and sulfide reference materials. It should be noted that the analytical conditions allowed us to detect oxygen down to a limit of 0.1 wt.%. Silicates were analyzed with 15kV and 15 nA and a 1–5 μm defocused beam, whereas silicate glasses were measured with 15 kV, 8 nA, and a 3 μm defocused beam. The following reference materials were used for calibration: silicates: forsterite (Si), diopside (Si, Mg, Ca), spessartine (Al, Mn), fayalite and andradite (Fe), Ni-metal (Ni), jadeite (Na), rutile (Ti), and Cr_2O_3 (Cr); silicate glasses: San Carlos olivine (Mg), BHVO-2G (Si, Al), orthoclase (K), wollastonite (Ca), fayalite (Fe), spessartine, (Mn), jadeite (Na), rutile (Ti), Cr_2O_3 (Cr), and chalcopyrite (S). The elements were measured on LIF (Fe, Cr, Mn, Ni, Cu), PET (S, Ti, Ca, K), TAP (Na, Mg, Si, Al), and PC1 (O) crystals. The major element contents of all phases are given in Tables S1 and S2 in Supporting Information S2 in the Electronic Annex.

3. Results

Five high-pressure and high-temperature experiments were conducted using the multi-anvil apparatus under quasi-hydrostatic conditions. Experiments E358 and E361, utilizing a harzburgitic matrix, primarily yielded Fo_{98} and Fo_{99} olivine, respectively, (up to 300 μm long) with traces of small (<5 μm) garnet (Figures 1a, 1b and 2a). Given the paucity of garnet in these experiments (<1 vol.%), we classify them as nominally monomineralic with respect to sulfide liquid wetting. In the harzburgitic experiments, the MgO capsules showed no indications of a chemical reaction with the starting materials. Experiment E390, conducted at 13 GPa, resulted in the crystallization of an eclogite composed of around 70 vol.% majoritic garnet ($Maj_{15}Prp_{48}Alm_{14}Grs_{21}Uv_1Sps_1$, 2–30 μm diameter) and 30 vol.% omphacitic clinopyroxene ($Di_{69}Jd_{29}Ae_2$, 5–40 μm diameter). Garnet crystals displayed euhedral to subhedral habits, while omphacite crystals were mostly subhedral. Majoritic garnet preserved primary phase relics, with Fe/Al-rich cores and Mg-rich rims that formed during the experiment. Despite the additional sintering step at 1350°C and 13 GPa for 20 hr, diffusion at sub-solidus conditions within the majoritic garnet did not entirely obliterate the garnet's primary composition ($Maj_1Prp_{56}Alm_{27}Grs_{13}Uv_1Sps_2$). However, the newly crystallized majoritic garnet is chemically homogeneous along the grain boundaries. The sulfide melt is found dispersed within the silicate interstitials, multi-grain junctions, and along grain boundaries (Figure 1e). In contrast to the harzburgitic experiments, a Fe-poor olivine shell approximately 20 μm thick developed between the sample and the inner capsule wall. This reaction minimally impacted the bulk chemical composition considering the total sample volume (800 μm in diameter and 700 μm in height). Importantly, the single crystal MgO capsule effectively retained the sulfide melt for the entire duration of the experiment, efficiently preventing its escape.

The experiments that were heated above the solidus of the eclogitic starting material (E392 and E394) contained a silicate melt that reacted with the MgO capsule forming Fe-poor olivine, Fo_{97} and Fo_{98}, respectively (Figure 2b). As a result, experiment E394 crystallized garnet and olivine but not omphacite, due to a deficit of SiO_2, which was consumed by the reaction with the MgO capsule forming olivine. The major components of the residual silicate melt are CaO (45(1) wt.%), SiO_2 (37.1(6) wt.%), and FeO^{total} (12.5(3) wt.%) (Table S1 in Supporting Information S2). The silicate melt is mostly located in the center of the capsule, reflecting the temperature gradient within the capsule. In experiment E392, where the eclogitic starting material completely melted, the silicate melt largely escaped from the capsule chamber, while the sulfide melt remained confined within the newly formed olivine matrix as large isolated melt blebs (Figure 1d).

3.1. Attainment of Equilibrium

Oxygen fugacity was not strictly controlled in our experiments, but rather buffered by the starting materials used. Based on the oxygen content of the sulfide melt, as well as the results from our previous study using similar starting materials and sample assemblies, we estimate that the oxygen fugacity was around $\log_{10}$ -3 relative to the fayalite-magnetite-quartz oxygen buffer (FMQ), which is close to what is expected in the ambient lithospheric

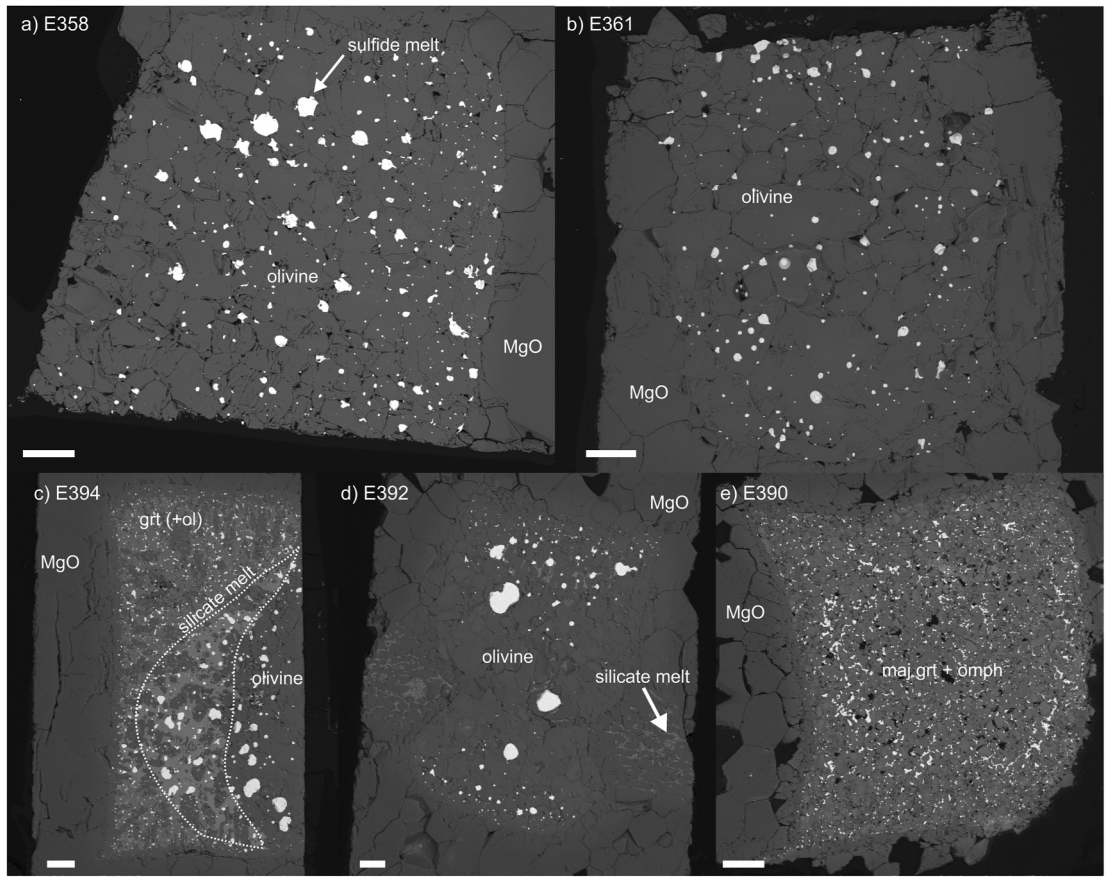

Figure 1. Back-scattered electron overview images of the studied samples. The bright phase in all experiments is the sulfide melt. (a) Experiment E358 conducted at 6 GPa with a harzburgite matrix and sulfide melt (Fe/Σmetals = 0.66). The sample mainly consists of olivine (Fo_{98}) with accessory garnet. (b) Experiment E361 run at the same conditions as E358 but with the more Ni-rich sulfide (Fe/Σmetals = 0.53). (c) Partial melting experiment E394, run at 7 GPa with a MORB glass and a Fe-rich sulfide (Fe/Σmetals = 0.90). The broken line marks the residual silicate melt. Olivine in the sample is formed by the reaction between the silicate melt and the MgO capsule. (d) Experiment E392, where the silicate starting material (Dora Maira eclogite) melted completely. The bulk of the melt reacted with the MgO and formed olivine (Fo_{97}). Some melt escaped the MgO capsule. (e) Experiment E390 that was conducted at 13 GPa with the Dora Maira eclogite plus Ni-rich sulfide (Fe/Σmetals = 0.53). Note, the ring of connected sulfide melt, that may have formed by zone refinement. The scale bars in the images are 100 μm.

mantle (Kress, 2007; Zhang et al., 2018). All experiments were conducted for a duration of 12 hr above the liquidus of the sulfide, based on the findings of Terasaki et al. (2005) who observed a stabilization of the dihedral angle within this time frame in the Fe-S melt and olivine system. However, achieving complete textural maturity in a high-Θ system within experimental time scales, as noted by Walte et al. (2007), presents challenges. The reasons are numerous and include pinning of grain boundaries by high-Θ liquid pockets and limited interaction of adjacent melt pockets. Some of the features discussed by Walte et al. (2007) are present in the experiments that show high Θ (E358 and E361) (Figure 2a). We observed evidence of abnormal grain growth, with melt pockets pinned at grain boundaries, and uneven distribution and size of melt pools, including large coalesced blebs and small dispersed blebs. Despite these observations, most of the melt blebs are well-rounded and exhibit high sphericity (e.g., E358: median Φ = 0.93(3)), suggesting a high degree of equilibration.

3.2. Apparent Dihedral Angles Between Silicates and Sulfide Melt

We measured 131 to 566 dihedral angles per experiment. The combined histograms and cumulative frequency diagrams illustrate the distribution of apparent dihedral angles within the samples (Figure 3). We also provide the median dihedral angle Θ and 95% confidence limits (Table 2). The mean and median dihedral angles are in excellent agreement (better than 1°) for all samples, except sample E390, which has a bimodal distribution of apparent angles. Consequently, the apparent angles show a normal distribution around the "true" dihedral angle. Experiments E358 and E361, which both used the same harzburgitic starting composition, exhibited similar mean

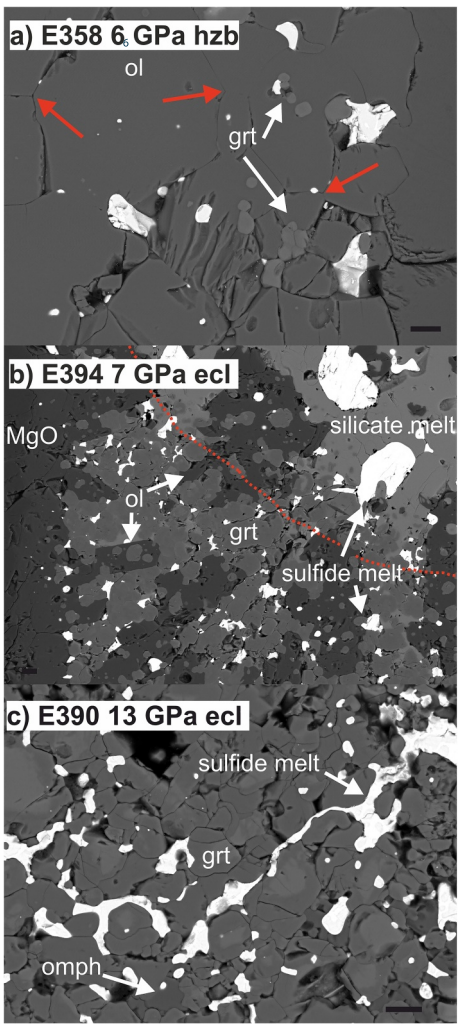

Figure 2. BSE detail images of three experiments. (a) Section of the experiment E358 carried out at 6 GPa with the harzburgite matrix. Highlighted are the garnets (white arrows). The sulfide melt migrated to form larger pockets, leaving dry triple junctions and isolated melt pockets along grain boundaries behind (red arrows). (b) This magnified image depicts the lower half of partial melting experiment E394 carried out at 7 GPa with a garnet plus olivine matrix. The broken red line separates the area dominated by the silicate melt (top right) from the solid silicates (garnet and olivine, lower left). The contrast in sulfide melt texture between the silicate melt zone and the solid silicate zone is evident. (c) This magnified area showcases the interconnected zone in experiment E390. In all experiments, the sulfide melt displays typical quench textures with Ni-Cu-rich domains. The black scale bars correspond to 10 μm in length.

dihedral angles Θ of 94° and 100°, respectively, despite containing sulfides with distinct atomic Fe/Σmetals of 0.66 and 0.53 (Table 2). The distribution of apparent dihedral angles is considerably broader in experiment E394, which crystallized garnet and olivine and also contains silicate melt. The mean apparent dihedral angle is 72° for the sulfide melt in contact with the silicate melt and the crystalline silicates. The apparent dihedral angle between the sulfide melt and the eclogite matrix of E390 is split into the median angle of the sulfide melt, forming a disseminated network (43°) and mostly isolated pockets (99°) (Figure 3) to account for the bimodal distribution of the apparent dihedral angles. Albeit the transition between the disseminated network and the isolated melt blebs is not always sharp, thus the representation of the wetting properties by two disparate dihedral angles better reflects the observed textures.

3.3. Tomography of the Sulfide Melt

Analysis through μCT indicates that the harzburgitic experiments E358 and E361 predominantly contain rounded melt pockets that are evenly distributed throughout the capsule, as illustrated in Figure 4 and supported by the median sphericity (0.93(2) and 0.96(1), respectively) (Table 3). The overwhelming majority of the sulfide melt blebs is isolated with over 95% of the melt blebs having a coordination number of 1 (Figure 6). The median melt pools size is 109(2) μm^3 and 121(2) μm^3. Within the studied range of Fe/Σmetals in the harzburgitic samples E358 (Fe/Σmetals = 0.55) and E361 (Fe/Σmetals = 0.66), the median melt pool size, melt pool volume distribution, sphericity, and network topology are almost identical (Figures 7 and 6).

In the experiments where the silicate partially (E394) or entirely (E392) melted, sulfide melt formed larger spheres (V > 1,500 μm^3) that became entrained in the silicate melt (E394) or olivine, which formed through the reaction of the silicate melt with the MgO capsule (E392 and E394). The shape of the sulfide melt in sample E394 was analyzed separately for the sulfide melt that resides in the garnet + olivine matrix and the sulfide melt fraction that is entrained in the silicate melt. In the garnet + olivine matrix, the median sulfide bleb volume is 133(2) μm^3, with a median Φ of 0.65(2). In contrast, for the sulfide melt in the silicate melt and newly formed olivine (sulfide melt marked yellow in Figure 5), the median sulfide bleb volume is 3,577(12) μm^3, with a median Φ of 0.88(1) The sulfide melt left behind in the unmelted fraction of the silicate host (E392) is trapped in the grain junctions and did not form larger blebs (Figure 5). The distribution of the coordination numbers of sample E394 is similar to the harzburgitic experiment E358, with 93% isolated nodes (Figure 6).

Sample E390 contains a finely dispersed (median melt pocket size: 24(2) μm^3) partially connected network of sulfide melt pools and branches with a median Φ of 0.57(1) (Figure 4). An interconnected network of sulfide melt occupies the outer third of the sample (Figure 2c). The observed structural features align with the concept of "disseminated networks" (Godel, 2013), where local network branches are terminated by melt blebs with high Θs. Moreover, the eclogitic sample E390 has the highest proportion of large, low-sphericity melt pools (Figure 7) and the largest fraction (>73%) of higher order nodes (coordination number ≥3) among all experiments. It is the only sample that shows interconnected melt pools (Figure 4). The median Φ of the 1% largest sulfide melt pools by volume (median volume = 4,254(261) μm^3) is 0.36(1), reflecting the branch-like structure and distorted shapes. Noteworthy is also its strong negative correlation between sphericity and melt pool volume (Figure 7).

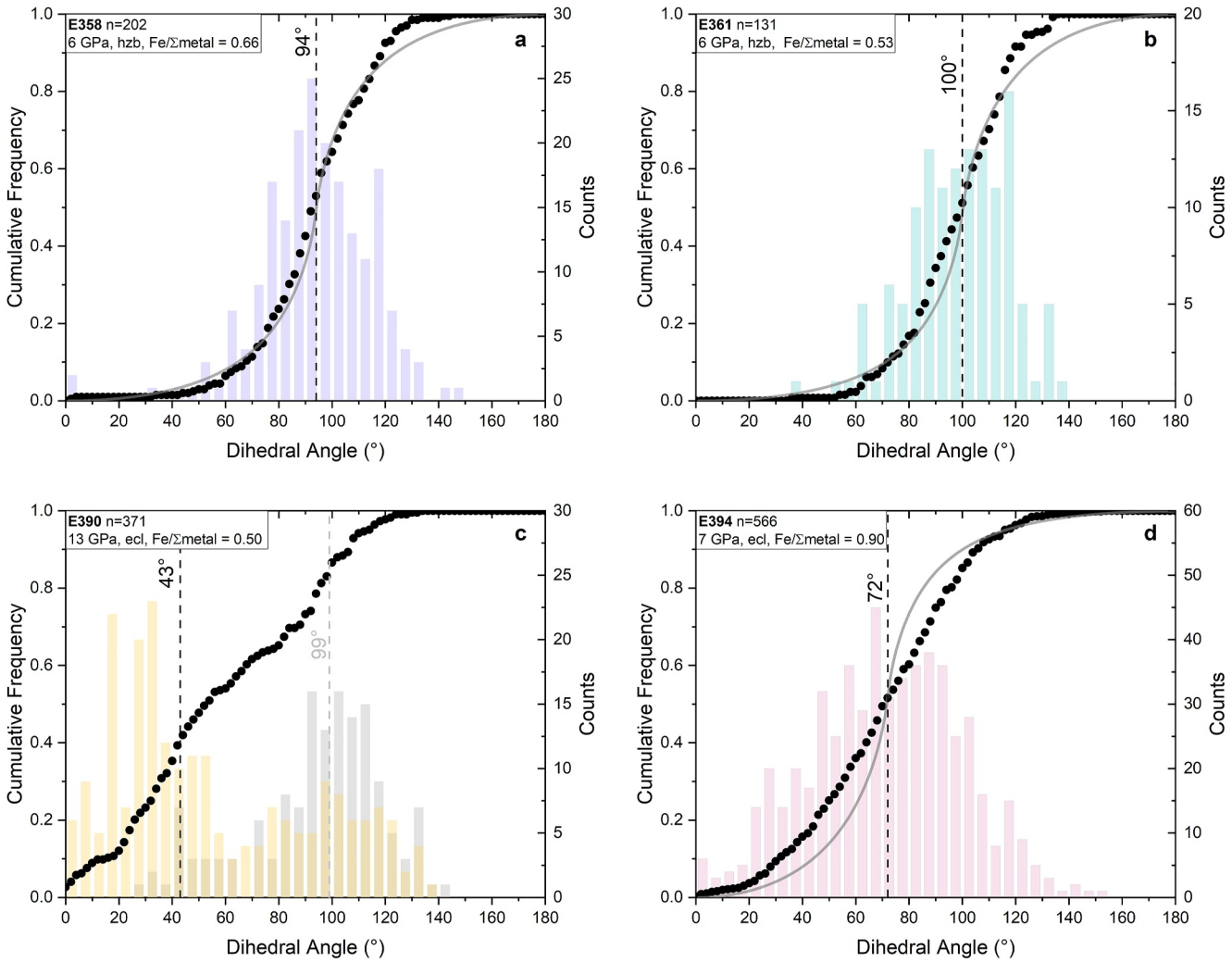

Figure 3. Combined histograms and cumulative distributions (depicted by black dots) illustrate the apparent dihedral angles of sulfide melt and the thin gray line the theoretical distribution around a unique "true" dihedral angle (Harker & Parker, 1945). In experiments where a single dihedral angle was observed, both the median and mean dihedral angles agree within 1°, allowing for the assumption of a normal distribution. The only exception is E390 (c), where the apparent dihedral angles exhibit a pronounced bimodal distribution. Here the angles were measured separately for the connected region and the isolated pockets in Figure 1e. Angle measurements were binned in 5° intervals, which reflect the measurement uncertainty as discussed in the text.

4. Discussion

4.1. Comparison to Previous Studies

The width of the distribution of the apparent dihedral angles is an indicator of the range of true dihedral angles in a sample. Any divergence from the theoretical distribution is related to one or more of the following parameters: anisotropy, strain, orientation, number of different phases in contact with the melt, and recrystallization (Harker & Parker, 1945; Jurewicz & Jurewicz, 1986; Walte et al., 2003; Yoshino & Watson, 2005). The cumulative distributions of apparent dihedral angles for the monomineralic samples E358 and E361 align with the theoretical predictions of a unique dihedral angle (Harker & Parker, 1945). The median dihedral angle for the monomineralic olivine bearing experiments E358 (Fo_{98}, O-in-melt 0.70(8) at.% O) and E361 (Fo_{99}, O-in-melt 0.61(4) at.% O) are within uncertainties to previous results obtained for olivine with a similar forsterite content and sulfide melt composition (oxygen content and cation-anion ratio) (Terasaki et al., 2005) (Figure 8). The µCT data and BSE image data collected for samples E358 and E361 clearly reveal heterogeneously distributed, isolated (96% isolated nodes), well-rounded (median Φ 0.93), and variably sized sulfide melt blebs. This suggests that the sulfide melt blebs were pinched off and either coalesced or grew through Ostwald ripening, resulting in some triple

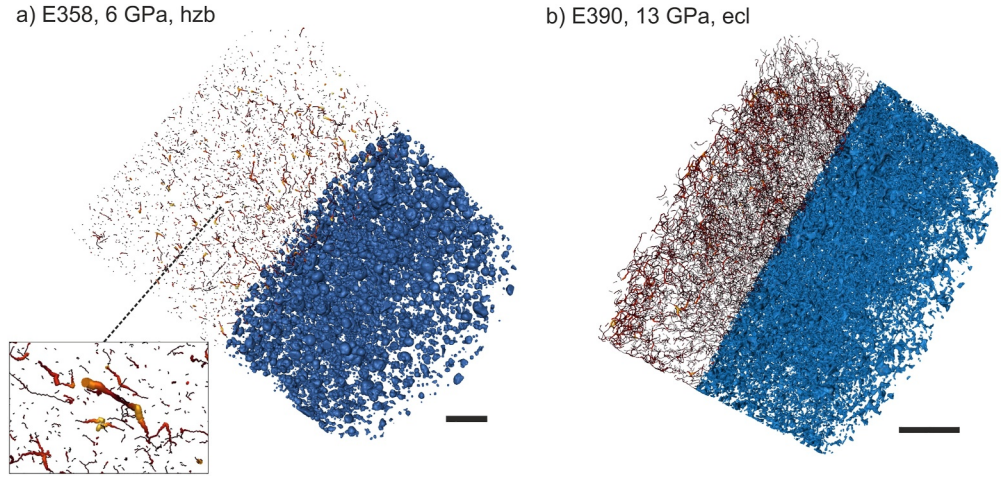

Figure 4. Combined volume renderings of sulfide melt and sulfide melt network, consisting of segments and nodes, using the skeleton toolbox in Avizo 2022.2. The nodes are not shown to improve readability. Displayed are the segments, which are color-coded by their thickness form yellow (thick) to brown (thin) (see left insert). (a) Mostly isolated nodes and short segments of the harzburgitic sample E358 (6 GPa). (b) Disseminated to highly connected network topology of experiment E390, conducted at 13 GPa with an eclogitic matrix. Blue colors represent the sulfide melt. The silicates are not shown to expose the sulfide melt. The black scale bars have a length of 100 μm.

junctions being depleted in melt while others are filled with sulfide melt. This behavior, typical for high Θ systems, has been previously observed by Yoshino and Watson (2005) in the FeS-olivine system, and has been interpreted to reflect free energy minimization. Our experiments in the matte-harzburgite system support previous findings (Walte et al., 2007) indicating that a significantly higher melt fraction is necessary to form an interconnected network of sulfide liquids in an olivine-dominated Earth's mantle.

Sample E394, which includes garnet, olivine, and silicate melt, exhibits a lower median dihedral angle of 72°, closer to the wetting threshold of 60°. The key distinguishing features are the presence of Ca-rich garnet (20.4(5) wt.% CaO), a silicate melt, and a Ni-poor sulfide melt (Fe/Σmetals = 0.90). Assuming the silicate melt does not exert a significant influence on the overall wetting properties of the sulfide melt (Holzheid et al., 2000), either the garnet, non-ferrous components, or crystal anisotropy have altered its wetting behavior. Given the wide range of measured angles and the deviation in width from the theoretical distribution around the median dihedral angle, we suggest that the sample contains more than one genuine dihedral angle, one for olivine and another for garnet. However, these angles are likely very similar, as they cannot be separated in the frequency distribution (Figure 3). Jurewicz and Jurewicz (1986) examined this theoretically and concluded that two genuine dihedral angles within 10° of each other are practically indistinguishable from a single dihedral angle with the averaged value of the two.

Table 3
Metrics Obtain From μCT Measurements

	Sphericity[a]	Volume [μm³]	Isolated nodes [%]
E358	0.93(3)	109(2)	96
E361	0.96(1)	121(2)	94
E390	0.57(1)	24(2)	19
E392		not measured	
E394 (with silicate melt)	0.88(1)	3,577(12)	93[b]
E394 (in grt + ol matrix)	0.65(1)	133(2)	

Note. Experiment 392 was not measured due to full melting of the starting materials (see text for discussion). The values reported for sphericity and volume are median values. Uncertainties are given in brackets as 1 standard error. [a]Only sulfide melt blebs above 300 μm³ were considered. [b]Overall node connectivity of sample E394.

It is worth noting that the observation of Jurewicz and Jurewicz (1986) is based on the assumption that the measurement uncertainty is the same for all samples. The amount of isolated nodes (93%) is similar to the harzburgite experiments (96%), which underscores that the sulfide melt is not connected. The melt blebs that are retained in the solid silicate matrix are finely dispersed, whereas the sulfide melt entrained in the silicate melt formed large and well-rounded blebs (median volume = 3,577(112) μm^3, Φ = 0.88(1) (Figures 5 and 7). This dichotomy can readily be explained by the differences in surface tension between sulfide melt and silicate melt, promoting the formation of spherical sulfide melt blebs suspended in the silicate melt (Holzheid, 2013). Finally, we cannot rule out the possibility that some sulfide blebs are covered by a thin (<1 μm width) silicate melt film, that would reduce the apparent dihedral angle of the melt pocket. The scenario would be similar to what Yoshino and Watson (2005) described in Figure 10d. Thus, the wetting angles obtained for experiment E394 set the minimum dihedral angle, in case a silicate melt film is present.

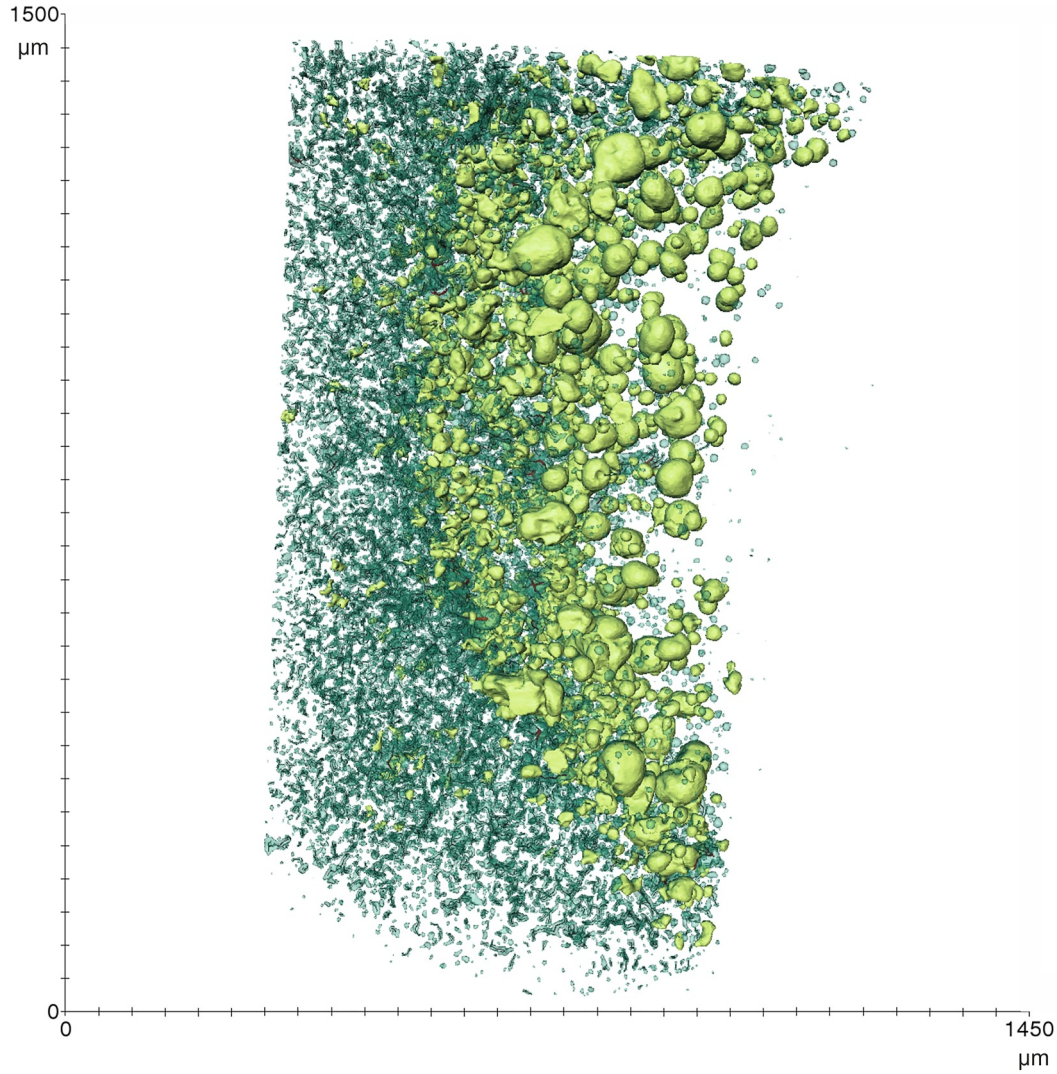

Figure 5. Tomographic reconstruction of partial melting experiment E394, conducted at 7 GPa with a garnet + olivine matrix and silicate melt. Categorization of the sulfide melt is based on melt pool volume ($V > 1{,}500\ \mu m^3$) and sphericity ($\Phi > 0.69$). These criteria predominantly distinguish the sulfide melt into two categories: Sulfide melt blebs (yellow) entrained in the silicate melt and newly formed olivine and sulfide melt blebs dispersed within the solid silicate matrix consisting of garnet and olivine (green). This highlights the dichotomy in sulfide melt texture, as in the BSE image showcased in Figure 1c.

4.2. The Effect of Pressure-Induced Changes in Mineralogy on Sulfide Melt Wetting Angles

In experiment E390 conducted at 13 GPa, significant deviations in sulfide melt topology, compared to other experiments, have been observed. The higher pressure, doubled from previous experiments, resulted in the crystallization of majoritic garnet and omphacite. In contrast to experiments conducted at lower pressures, smaller sulfide melt blebs connected and formed larger melt networks, as evidenced by the high fraction of non-spherical ($\Phi = 0.36(1)$) and large (median volume 4,254 (261) μm^3), branched melt pools. Notably, the largest 1%, in terms of melt bleb volume, of the sulfide melt constitutes 57% of the total melt volume. Since the sulfide starting material was identical to experiments E358 and E361, we attribute the changes in melt topology to the pressure-induced change in silicate mineralogy rather than the effect of pressure in isolation. This view is reinforced by a previous study by Terasaki et al. (2005), who have argue that pressure does not notably affect the dihedral angle of sulfide melts with olivine and its polymorphs within a range of 3.5–20 GPa. However, the same study also highlighted the role of oxygen in the sulfide melt, demonstrating that increased oxygen content decreases the dihedral angle due to its influence on the surface energy of the melt. Our experiments encompass a narrow range of oxygen concentrations in the sulfide melt (0.62(3)-1.9(3) at.% O). Although the observed decrease in the

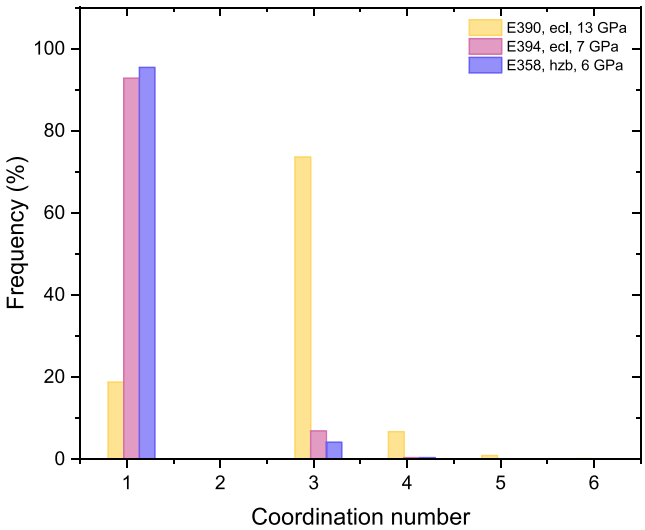

Figure 6. Relative distribution of the coordination number of network nodes in the three most distinct samples. The absence of 2-fold coordinated nodes can be explained by the fact that sulfide blebs commonly occupy the junctions where three or more grains meet, hence a node connected only on two ends is unlikely. A similar distribution of coordination numbers was also reported by Godel (2013) for natural sulfides.

dihedral angle from 94° (0.70(8) at.% O) and 100° (0.62(3) at.% 0) to 72° (1.9 (3) at.% O) mirrors the trend observed in previous studies, notably that depicted in Figure 3 of Terasaki et al. (2005), this trend does not entirely apply to experiment E390, where the sulfide melt contained only 1.7(3) at.% O. According to Terasaki et al. (2005), and references therein, the mean dihedral angle should be above the connectivity threshold of 60° at pressures between 4.6 and 11 GPa at the given cation-anion ratio of <1 (Table S2 in Supporting Information S2). Consequently, we attribute the decrease in the dihedral angle, particularly for the connected fraction of the sample (43°), and the higher node connectivity (Figure 4) to pressure-induced changes in mineralogy. The continuous transition from garnet to majorite and Na-Al pyroxenes with pressure makes the deconvolution of the specific effects of pressure from those of altered mineralogy challenging. Despite this, our findings underscore the complex interplay between pressure, mineralogy, and oxygen concentration in shaping the behavior of sulfide melt mobility under high-pressure conditions.

4.3. Comparison of 2D and 3D Metrics to Describe Liquid Connectivity

The mean dihedral angle proves effective in analyzing two-component systems comprising a solid and a liquid phase. However, its accuracy decreases when characterizing sulfide melt behavior within complex mineral assemblages, particularly when net interfacial energy ratios differ among the solid matrix phases and the liquid phase. This discrepancy becomes apparent in relative frequency plots, which deviate from a normal distribution and reveal multiple local maxima, as discussed by Jurewicz and Jurewicz (1986). When two or more dihedral angles resemble each other (i.e., within in 10° to each other (Jurewicz & Jurewicz, 1986)), this result in a broader distribution of apparent dihedral angles compared to the theoretically predicted distribution of a unique dihedral angle. Consequently, the apparent mean dihedral angle derived from this wider distribution fails to accurately represent the dihedral angles within a polymineralic system (Jurewicz & Jurewicz, 1986). Additionally, anisotropy can produce a similar effect on the distribution of dihedral angles. Therefore, the crystal orientation of highly anisotropic minerals (e.g., clinopyroxene) must also be considered. In summary, the 2D and 3D textures exhibit a general agreement. However, μCT provides a more comprehensive insight into sulfide melt connectivity compared to solely relying on the measurement of a single mean dihedral angle. The assessment of μCT data better addresses the complexities of inhomogeneous melt topologies (E390) and melt bleb size distributions (E394). These additional parameters are crucial for discerning differences among sulfide melts in various lithologies and will improve our understanding of the sulfur cycle in deep Earth's interior. The robustness of the 3D parameters hinges on the achievable resolution of the μCT-scans. By using ultra nano-CT, Berg et al. (2017) demonstrated that even finest, that is, a few micron-sized liquid networks can be analyzed reliably.

4.4. Implications for the Mobility of Sulfur and the Metasomatic Potential of Sulfide Liquids in the Mantle

The interaction between sulfide melts and peridotitic mineral matrices presents a complex picture, evident in the highly variable highly siderophile element (HSE) systematics and Pt-Re-Os isotope records of accessory sulfide grains found in peridotite xenoliths. Recent advancements in microsampling and analytical techniques have unveiled multiple sulfide populations within single peridotite samples. For instance, studies by Bragagni et al. (2017) and Wainwright et al. (2015) identified up to four sulfide generations in xenoliths from Letlhakane (Botswana) and Rae (Canada) cratons, based on Os isotope compositions and HSE systematics. Even enclosed sulfides, typically deemed primary (i.e., non-metasomatic), often exhibit signs of cryptic metasomatism, as observed in Letlhakane kimberlite by Wainwright et al. (2015). However, the precise mechanisms behind sulfide-driven metasomatism remain elusive, particularly regarding how sulfide introduces its chalcophile and HSE elemental load to a host mantle rock. Understanding this process is crucial for accurately interpreting geochemical data from metasomatized mantle lithologies, especially for the precision of Os model ages recording pulses of mantle melting, which are closely associated with primary sulfides (Lorand & Luguet, 2016; Luguet et al., 2008; Luguet & Reisberg, 2016).

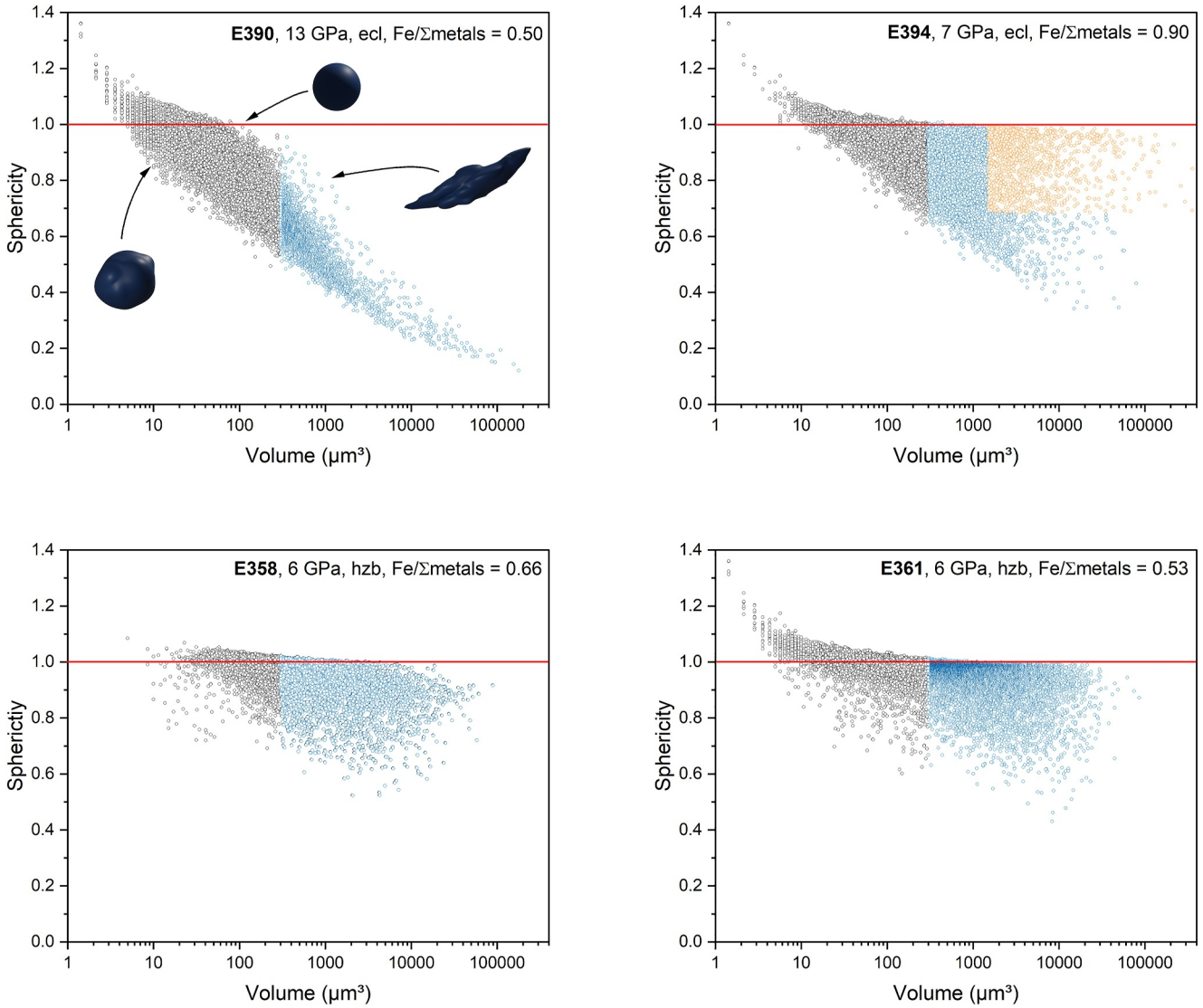

Figure 7. Sphericity Φ shown as a function of sulfide melt bleb volume. In the upper left subfigure, three exemplary objects for different degrees of sphericity are shown. The blebs that were considered for the calculation of Φ are highlighted in blue. The melt spheres that were classified as suspended in the silicate melt in sample E394 are marked in orange. Be aware that the criteria for bleb volume and sphericity do not encompass 100% of the sulfide blebs associated with the silicate melt. However, they provide a strong initial assessment. The red line marks a Φ of 1, which represents a perfect sphere.

Our findings highlight the complexities involved in initiating sulfide melt percolation in the mantle, narrowing down the conditions where this process occurs. In regions where subducted oceanic crust transforms into eclogite and garnetite at increasing depths (Akaogi & Akimoto, 1977; Green & Ringwood, 1967), sulfide melts percolate through these lithologies, even at small modal fractions (<5 vol.% critical threshold), regardless of the presence of fluids or silicate melts. However, in the more depleted upper mantle, sulfide melts become trapped along grain boundaries due to high dihedral angles and low modal fractions (<0.1 wt. %) (Palme & O'Neill, 2014). Even in garnet-bearing lithologies like eclogites, the range of P-T conditions allowing sulfide melt mobility is limited, despite some eclogites (e.g., Roberts Victor eclogite, South Africa) having substantially higher sulfide modal abundances (up to 2 wt.%) compared to the more depleted mantle (Gréau et al., 2013). Solid crystalline sulfides remain stable up to 6 GPa and 1250°C (Beyer et al., 2022). Above 6 GPa, eclogitic sulfides begin to partially melt, reaching full melting when the sulfide liquidus intersects the mantle adiabat at approximately 14 GPa (Beyer et al., 2022). Our results indicate that eclogitic sulfides are more likely to percolate in an eclogitic matrix above the minimum melting pressure of 6 GPa, especially toward the higher end of the partial melting interval (i.e., at 14 GPa), where garnet has a higher proportion of majorite. Recent research by Zou et al. (2024) supports our

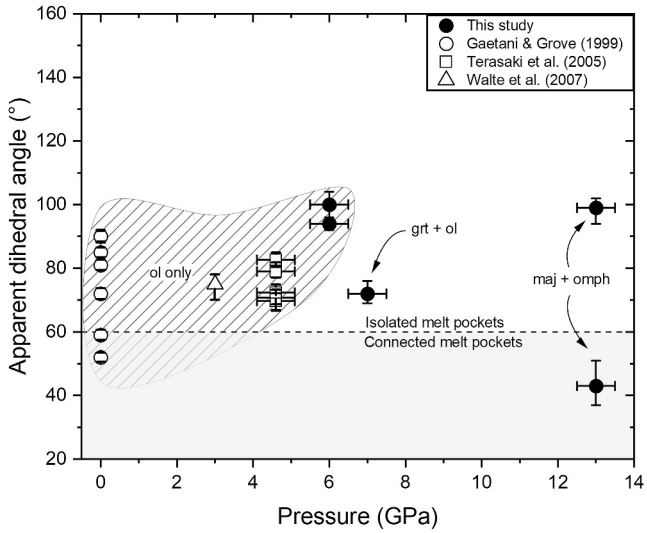

Figure 8. Median apparent dihedral angles for this studies and other studies (Gaetani & Grove, 1999; Rose & Brenan, 2001; Terasaki et al., 2005) with similar sulfide melt cation-anion ratios. The spread in the data of Gaetani and Grove (1999) can readily explained by variations in the oxygen content of the melt. Uncertainties in pressure are based on pressure calibrations and the uncertainties in the dihedral angle represent the 95% confidence level of the median dihedral angle. If not labeled differently, the symbols correspond to sulfide melt—olivine Θs.

expectations, attributing the low chalcophile element abundances in primitive eclogite partial melts from Hannuoba (eastern China) to their retention in subducted oceanic crust deep within the mantle. The persistence of sulfide down to transition zone pressures would indeed facilitate the retention of chalcophile elements in subducted oceanic crust, a notion supported by our data.

At first glance, sulfide melts appear capable of percolating through eclogitic host lithologies at pressures near the transition zone and temperatures close to the mantle adiabat. However, according to our findings, any sulfide melt percolating through an eclogitic matrix would halt upon reaching the overlying depleted mantle material. This is due to the high dihedral angles between the sulfide melt and the olivine-pyroxene matrix, coupled with the unlikelihood of reaching modal abundances high enough to attain the critical threshold value of 5 vol. %. It is thus apparent that, on its own, sulfide melt has only a limited ability to percolate in the sub-lithospheric mantle, and thus is equally limited to exchange chalcophile elements and HSE pervasively. This observation contrasts with findings in peridotite xenoliths, which consistently demonstrate disruption of chalcophile and HSE systematics associated with sulfide mineralogy (Lorand & Luguet, 2016; Luguet et al., 2008; Luguet & Reisberg, 2016). However, it is widely recognized that sulfide-driven metasomatism typically occurs alongside silicate melt percolation and the concurrent recrystallization of the host peridotite (Hart & Gaetani, 2016; Harvey et al., 2010; Lorand & Luguet, 2016; Luguet & Reisberg, 2016). Based on our study results, especially the observed coalescence and aggregation of sulfide melt droplets in the silicate melt from experiment E394 (Figure 5), it seems increasingly probable that sulfide-driven metasomatism relies on the presence of silicate melt or, in its absence, a sulfur-bearing fluid. It is however, improbable that such metasomatism can take place through percolation of sulfide melt alone. Finally, any kind of deformation that takes place in dynamic tectonic settings (e.g., subducting slabs), will incTrease the likelihood of melt percolation (Berg et al., 2017; Shi et al., 2013; Wang et al., 2020). Thus, our results set the upper limits for melt percolation.

Data Availability Statement

All data used in this study are either provided in the electronic annex or are freely available in the YODA repository of Utrecht University (Beyer et al., 2024). The 3D figures were created using Avizo 2022.2. All other figures were done in Origin Pro 2023b.

Acknowledgments
ROCF and CB are grateful for financial support from the Deutsche Forschungsgemeinschaft (via Grants BE 6053/2–1 and FO 698/13–1). The authors also thank Nils Jöns and Sabine Weisel for their assistance during EMPA measurements at the Ruhr-University Bochum. The manuscript was improved by the constructive suggestions from Paul D. Asimow, ZhangZhou J, and an anonymous reviewer. The Ghent University Special Research Fund (BOF-UGent) is acknowledged to support the UGent Core facility UGCT (BOF.COR.2022.0009). Lastly, this project has received funding from the European Union's Horizon 2020 research and innovation program under grant agreement No 101005611 for Transnational Access conducted at Ghent University. Open Access funding enabled and organized by Projekt DEAL.

References

Akaogi, M., & Akimoto, S. (1977). Pyroxene-garnet solid-solution equilibria in the systems $Mg_4Si_4O_{12}$ $Mg_3Al_2Si_3O_{12}$ and $Fe_4Si_4O_{12}$ $Fe_3Al_2Si_3O_{12}$ at high pressures and temperatures. *Physics of the Earth and Planetary Interiors*, *15*(1), 90–106. https://doi.org/10.1016/0031-9201(77)90013-9

Bagdassarov, N., Golabek, G. J., Solferino, G., & Schmidt, M. W. (2009). Constraints on the Fe–S melt connectivity in mantle silicates from electrical impedance measurements. *Physics of the Earth and Planetary Interiors*, *177*(3–4), 139–146. https://doi.org/10.1016/j.pepi.2009.08.003

Ballhaus, C., & Ellis, D. J. (1996). Mobility of core melts during Earth's accretion. *Earth and Planetary Science Letters*, *143*(1–4), 137–145. https://doi.org/10.1016/0012-821x(96)00135-5

Barnes, S. J., Fiorentini, M. L., Austin, P., Gessner, K., Hough, R. M., & Squelch, A. P. (2008). Three-dimensional morphology of magmatic sulfides sheds light on ore formation and sulfide melt migration. *Geology*, *36*(8), 655–658. https://doi.org/10.1130/G24779A.1

Berg, M. T. L., Bromiley, G. D., Butler, I. B., Frost, M., Bradley, R., Carr, J., et al. (2017). Deformation-aided segregation of Fe-S liquid from olivine under deep Earth conditions: Implications for core formation in the early solar system. *Physics of the Earth and Planetary Interiors*, *263*, 38–54. https://doi.org/10.1016/j.pepi.2017.01.004

Beyer, C., Bissbort, T., Hartmann, R., Berndt, J., Klemme, S., & Fonseca, R. O. C. (2022). High-pressure phase relations in the system Fe–Ni–Cu–S up to 14 GPa: Implications for the stability of sulfides in the Earth's upper mantle. *Contributions to Mineralogy and Petrology*, *177*(10), 99. https://doi.org/10.1007/s00410-022-01966-x

Beyer, C., Fonseca, R. O. C., Bissbort, T., Schröer, L., & Cnudde, V. (2024). Sulfide melt wetting properties in Earth's mantle: New constraints from combined 2D and 3D imaging [Dataset]. *Uttrecht: YODA*. https://doi.org/10.24416/UU01-RPULDA

Beyer, C., Myhill, R., Marquardt, K., & McCammon, C. A. (2021). A reversed redox gradient in Earth's mantle transition zone. *Earth and Planetary Science Letters*, *575*, 117181. https://doi.org/10.1016/j.epsl.2021.117181

Bragagni, A., Luguet, A., Fonseca, R., Pearson, D., Lorand, J.-P., Nowell, G., & Kjarsgaard, B. (2017). The geological record of base metal sulfides in the cratonic mantle: A microscale $^{187}OS/^{188}OS$ study of peridotite xenoliths from Somerset Island, Rae Craton (Canada). *Geochimica et Cosmochimica Acta*, *216*, 264–285. https://doi.org/10.1016/j.gca.2017.04.015

Brenan, J. M., & Rose, L. A. (2002). Experimental constraints on the wetting of chromite by sulfide liquid. *The Canadian Mineralogist*, *40*(4), 1113–1126. https://doi.org/10.2113/gscanmin.40.4.1113

Cerantola, V., Walte, N. P., & Rubie, D. C. (2015). Deformation of a crystalline olivine aggregate containing two immiscible liquids: Implications for early core–mantle differentiation. *Earth and Planetary Science Letters*, *417*, 67–77. https://doi.org/10.1016/j.epsl.2015.02.014

Dierick, M., Van Loo, D., Masschaele, B., Van den Bulcke, J., Van Acker, J., Cnudde, V., & Van Hoorebeke, L. (2014). Recent micro-CT scanner developments at UGCT. *Nuclear Instruments and Methods in Physics Research Section B: Beam Interactions with Materials and Atoms*, *324*, 35–40. https://doi.org/10.1016/j.nimb.2013.10.051

Fonseca, R. O. C., Beyer, C., Bissbort, T., Hartmann, R., & Schuth, S. (2024). Partitioning of highly siderophile elements between monosulfide solid solution and sulfide melt at high pressures. *Contributions to Mineralogy and Petrology*, *179*(2), 17. https://doi.org/10.1007/s00410-023-02092-y

Gaetani, G. A., & Grove, T. L. (1999). Wetting of mantle olivine by sulfide melt: Implications for Re/Os ratios in mantle peridotite and late-stage core formation. *Earth and Planetary Science Letters*, *169*(1–2), 147–163. https://doi.org/10.1016/s0012-821x(99)00062-x

Gilpin, L., Draper, D., Chabot, N., Schwandt, C., & Agee, C. (2002). Metal and silicate melt mobility in garnet-rich solid matrices: Implications for Martian differentiation. In *33rd annual lunar and planetary science conference* (Vol. 1140).

Godel, B. (2013). High-resolution X-ray computed tomography and its application to ore deposits: From data acquisition to quantitative three-dimensional measurements with case studies from Ni-Cu-PGE deposits. *Economic Geology*, *108*(8), 2005–2019. https://doi.org/10.2113/econgeo.108.8.2005

Godel, B., Barnes, S.-J., & Maier, W. D. (2006). 3-D distribution of sulphide minerals in the Merensky Reef (Bushveld Complex, South Africa) and the JM Reef (Stillwater Complex, USA) and their relationship to microstructures using X-ray computed tomography. *Journal of Petrology*, *47*(9), 1853–1872. https://doi.org/10.1093/petrology/egl029

Gréau, Y., Alard, O., Griffin, W. L., Huang, J.-X., & O'Reilly, S. Y. (2013). Sulfides and chalcophile elements in Roberts Victor eclogites: Unravelling a sulfide-rich metasomatic event. *Chemical Geology*, *354*, 73–92. https://doi.org/10.1016/j.chemgeo.2013.06.015

Green, D. H., & Ringwood, A. E. (1967). An experimental investigation of the gabbro to eclogite transformation and its petrological applications. *Geochimica et Cosmochimica Acta*, *31*(5), 767–833. https://doi.org/10.1016/s0016-7037(67)80031-0

Groebner, N., & Kohlstedt, D. L. (2006). Deformation-induced metal melt networks in silicates: Implications for core–mantle interactions in planetary bodies. *Earth and Planetary Science Letters*, *245*(3), 571–580. https://doi.org/10.1016/j.epsl.2006.03.029

Harker, D., & Parker, E. R. (1945). Grain shape and grain growth. *Transactions of the American Society of Metals*, *34*, 156–195.

Hart, S. R., & Gaetani, G. A. (2016). Experimental determination of Pb partitioning between sulfide melt and basalt melt as a function of P, T and X. *Geochimica et Cosmochimica Acta*, *185*, 9–20. https://doi.org/10.1016/j.gca.2016.01.030

Harvey, J., Gannoun, A., Burton, K., Schiano, P., Rogers, N., & Alard, O. (2010). Unravelling the effects of melt depletion and secondary infiltration on mantle Re–Os isotopes beneath the French Massif Central. *Geochimica et Cosmochimica Acta*, *74*(1), 293–320. https://doi.org/10.1016/j.gca.2009.09.031

Holzheid, A. (2013). Sulphide melt distribution in partially molten silicate aggregates: Implications to core formation scenarios in terrestrial planets. *European Journal of Mineralogy*, *25*(3), 267–277. https://doi.org/10.1127/0935-1221/2013/0025-2264

Holzheid, A., Sylvester, P., O'Neill, H. S. C., Rubie, D. C., & Palme, H. (2000). Evidence for a late chondritic veneer in the Earth's mantle from high pressure partitioning of palladium and platinum. *Nature*, *406*(6794), 396–399. https://doi.org/10.1038/35019050

Irifune, T. (1987). An experimental investigation of the pyroxene-garnet transformation in a pyrolite composition and its bearing on the constitution of the mantle. *Physics of the Earth and Planetary Interiors*, *45*(4), 324–336. https://doi.org/10.1016/0031-9201(87)90040-9

Jurewicz, S. R., & Jurewicz, A. J. G. (1986). Distribution of apparent angles on random sections with emphasis on dihedral angle measurements. *Journal of Geophysical Research*, *91*(B9), 9277–9282. https://doi.org/10.1029/JB091iB09p09277

Kono, Y., Kuwahara, H., Gréaux, S., Rivers, M. L., Wang, Y., Higo, Y., et al. (2023). Strong effect of liquid Fe–S on elastic wave velocity of olivine aggregate: Implication for the low velocity anomaly at the base of the lunar mantle. *Earth and Planetary Science Letters*, *618*, 118287. https://doi.org/10.1016/j.epsl.2023.118287

Kress, V. (2007). Thermochemistry of sulfide liquids III: Ni-bearing liquids at 1 bar. *Contributions to Mineralogy and Petrology*, *154*(2), 191–204. https://doi.org/10.1007/s00410-007-0187-7

Lorand, J.-P., & Luguet, A. (2016). Chalcophile and siderophile elements in mantle rocks: Trace elements controlled by trace minerals. *Reviews in Mineralogy and Geochemistry*, *81*(1), 441–488. https://doi.org/10.1515/9781501502095-010

Luguet, A., Lorand, J.-P., & Seyler, M. (2003). Sulfide petrology and highly siderophile element geochemistry of abyssal peridotites: A coupled study of samples from the Kane Fracture Zone (45°W 23° 20N, MARK area, Atlantic Ocean). *Geochimica et Cosmochimica Acta*, *67*(8), 1553–1570. https://doi.org/10.1016/s0016-7037(02)01133-x

Luguet, A., Pearson, D. G., Nowell, G. M., Dreher, S. T., Coggon, J. A., Spetsius, Z. V., & Parman, S. W. (2008). Enriched Pt-Re-Os isotope systematics in plume lavas explained by metasomatic sulfides. *Science*, *319*(5862), 453–456. https://doi.org/10.1126/science.1149868

Luguet, A., & Reisberg, L. (2016). Highly siderophile element and ^{187}Os signatures in non–cratonic basalt–hosted peridotite xenoliths: Unravelling the origin and evolution of the post-Archean lithospheric mantle. *Reviews in Mineralogy and Geochemistry*, *81*(1), 305–367. https://doi.org/10.2138/rmg.2016.81.06

Miller, K. J., Zhu, W.-L., Montési, L. G. J., & Gaetani, G. A. (2014). Experimental quantification of permeability of partially molten mantle rock. *Earth and Planetary Science Letters*, *388*, 273–282. https://doi.org/10.1016/j.epsl.2013.12.003

Minarik, W. G., Ryerson, F. J., & Watson, E. B. (1996). Textural entrapment of core-forming melts. *Science*, *272*(5261), 530–533. https://doi.org/10.1126/science.272.5261.530

Palme, H., & O'Neill, H. S. C. (2014). Cosmochemical estimates of mantle composition. In *Treatise on geochemistry* (2nd ed., pp. 15–36). Elsevier.

Roberts, J. J., Kinney, J. H., Siebert, J., & Ryerson, F. J. (2007). Fe-Ni-S melt permeability in olivine: Implications for planetary core formation. *Geophysical Research Letters*, *34*(14), L14306. https://doi.org/10.1029/2007GL030497

Rose, L. A., & Brenan, J. M. (2001). Wetting properties of Fe-Ni-Co-Cu-OS melts against olivine: Implications for sulfide melt mobility. *Economic Geology*, *96*(1), 145–157. https://doi.org/10.2113/gsecongeo.96.1.145

Rubie, D. C. (1999). Characterising the sample environment in multianvil high-pressure experiments. *Phase Transitions*, *68*(3), 431–451. https://doi.org/10.1080/01411599908224526

Schindelin, J., Arganda-Carreras, I., Frise, E., Kaynig, V., Longair, M., Pietzsch, T., et al. (2012). Fiji: An open-source platform for biological-image analysis. *Nature Methods*, *9*(7), 676–682. https://doi.org/10.1038/nmeth.2019

Shannon, M. C., & Agee, C. B. (1996). High pressure constraints on percolative core formation. *Geophysical Research Letters*, *23*(20), 2717–2720. https://doi.org/10.1029/96GL02817

Shannon, M. C., & Agee, C. B. (1998). Percolation of core melts at lower mantle conditions. *Science*, *280*(5366), 1059–1061. https://doi.org/10.1126/science.280.5366.1059

Shi, C. Y., Zhang, L., Yang, W., Liu, Y., Wang, J., Meng, Y., et al. (2013). Formation of an interconnected network of iron melt at Earth's lower mantle conditions. *Nature Geoscience*, *6*(11), 971–975. https://doi.org/10.1038/ngeo1956

Terasaki, H., Frost, D. J., Rubie, D. C., & Langenhorst, F. (2005). The effect of oxygen and sulphur on the dihedral angle between Fe–O–S melt and silicate minerals at high pressure: Implications for Martian core formation. *Earth and Planetary Science Letters*, *232*(3–4), 379–392. https://doi.org/10.1016/j.epsl.2005.01.030

Terasaki, H., Frost, D. J., Rubie, D. C., & Langenhorst, F. (2008). Percolative core formation in planetesimals. *Earth and Planetary Science Letters*, *273*(1), 132–137. https://doi.org/10.1016/j.epsl.2008.06.019

von Bargen, N., & Waff, H. S. (1986). Permeabilities, interfacial areas and curvatures of partially molten systems: Results of numerical computations of equilibrium microstructures. *Journal of Geophysical Research*, *91*(B9), 9261–9276. https://doi.org/10.1029/jb091ib09p09261

Wadell, H. (1935). Volume, shape, and roundness of quartz particles. *The Journal of Geology*, *43*(3), 250–280. https://doi.org/10.1086/624298

Walte, N. P., Becker, J. K., Bons, P. D., Rubie, D. C., & Frost, D. J. (2007). Liquid-distribution and attainment of textural equilibrium in a partially-molten crystalline system with a high-dihedral-angle liquid phase. *Earth and Planetary Science Letters*, *262*(3–4), 517–532. https://doi.org/10.1016/j.epsl.2007.08.003

Walte, N. P., Bons, P. D., Passchier, C. W., & Koehn, D. (2003). Disequilibrium melt distribution during static recrystallization. *Geology*, *31*(11), 1009–1012. https://doi.org/10.1130/G19815.1

Wang, W., Huang, S., Huang, F., Zhao, X., & Wu, Z. (2020). Equilibrium inter-mineral titanium isotope fractionation: Implication for high-temperature titanium isotope geochemistry. *Geochimica et Cosmochimica Acta*, *269*, 1137–1170. https://doi.org/10.1016/j.gca.2019.11.008

Yoshino, T., Walter, M. J., & Katsura, T. (2003). Core formation in planetesimals triggered by permeable flow. *Nature*, *422*(6928), 154–157. https://doi.org/10.1038/nature01459

Yoshino, T., & Watson, E. B. (2005). Growth kinetics of FeS melt in partially molten peridotite: An analog for core-forming processes. *Earth and Planetary Science Letters*, *235*(1), 453–468. https://doi.org/10.1016/j.epsl.2005.04.021

Zhang, Z., & Hirschmann, M. M. (2016). Experimental constraints on mantle sulfide melting up to 8 GPa. *American Mineralogist*, *101*(1), 181–192. https://doi.org/10.2138/am-2016-5308

Zhang, Z., von der Handt, A., & Hirschmann, M. M. (2018). An experimental study of Fe–Ni exchange between sulfide melt and olivine at upper mantle conditions: Implications for mantle sulfide compositions and phase equilibria. *Contributions to Mineralogy and Petrology*, *173*(3), 1–18. https://doi.org/10.1007/s00410-018-1444-7

Zou, Z., Wang, Z., Xu, Y.-G., Foley, S., Cheng, H., Ma, L., et al. (2024). Deep mantle cycle of chalcophile metals and sulfur in subducted oceanic crust. *Geochimica et Cosmochimica Acta*, *370*, 15–28. https://doi.org/10.1016/j.gca.2024.02.007